Testing Stationarity and Statistical Independence of Multistatic/Polarimetric Sea-Clutter With Application to NetRAD Data

Augusto Aubry, *Senior Member, IEEE*, Vincenzo Carotenuto, *Senior Member, IEEE*, Antonio De Maio, *Fellow, IEEE*, and Francesco Fioranelli, *Senior Member, IEEE*

***Abstract*— The design of bespoke adaptive detection schemes relying on the joint use of multistatic/polarimetric measurements requires a preliminary statistical inference on the clutter interference environment. This is of paramount importance to develop an analytic model for the received signal samples, which is mandatory for the synthesis of radar detectors. In this respect, the aim of this article is the development of suitable learning tools to study some important statistical features of the sea-clutter environment perceived at the nodes of a multistatic/polarimetric radar system. Precisely, the stationarity of the data in the slow-time domain is first assessed by resorting to generalized inner product (GIP) based statistics. Then, the possible presence of structural symmetries in the clutter covariance matrices is investigated. Finally, relationships between some statistical parameters characterizing the sea-clutter returns on the bistatic polarimetric channels are explored via specific sequential hypothesis testing. This research activity is complemented by the use of radar returns measured via the netted RADar (NetRAD), which collects simultaneously monostatic and bistatic polarimetric measurements. The results indicate that the analyzed data can be modeled as drawn from a stationary Gaussian process within the coherence time. In addition, the bistatic returns on the different polarimetric channels can be assumed statistically independent with speckle components possibly exhibiting proportional/equal covariance matrices depending on the transmit/receive polarization and bistatic geometry.**

***Index Terms*— Covariance matrix structure, data homogeneity, generalized inner product (GIP), model order selection (MOS), multistatic/polarimetric radar, proportionality/equality of covariance matrices, sea-clutter, spherically invariant random process (SIRP).**

Manuscript received 22 September 2023; revised 5 January 2024; accepted 2 February 2024. Date of publication 6 February 2024; date of current version 26 February 2024. The work of Augusto Aubry and Antonio De Maio was supported in part by the European Union under the Italian National Recovery and Resilience Plan (NRRP) of NextGenerationEU, partnership on "Telecommunications of the Future" (CUP J33C22002880001, PE00000001 - program RESTART). The work of Vincenzo Carotenuto was supported by the Research Program PON Research and Innovation AIM1878982-1. An earlier version of this paper was presented at the 10th IEEE International Workshop on Metrology for AeroSpace (MetroAeroSpace) [DOI: 10.1109/MetroAeroSpace57412.2023.10190048]. *(Corresponding author: Vincenzo Carotenuto.)*

Augusto Aubry, Vincenzo Carotenuto, and Antonio De Maio are with Department of Electrical Engineering and Information Technologies, University of Naples Federico II, 80125 Naples, Italy (e-mail: augusto.aubry@unina.it; vincenzo.carotenuto@unina.it; ademaio@unina.it).

Francesco Fioranelli is with the Department of Microelectronics, Delft University of Technology, 2628 CD Delft, The Netherlands (e-mail: f.fioranelli@tudelft.nl).

Digital Object Identifier 10.1109/TGRS.2024.3362872

I. Introduction

THE design of adaptive detection schemes calls for a preliminary statistical inference on the clutter interference environment. This is essential for developing a well-suited analytic model for the received signal, necessary to synthesize taylored coherent radar detectors. Indeed, incorrect modeling of the clutter environment can lead to false and/or missed detections, compromising the overall accuracy and effectiveness of a radar system [1], [2], [3], [4], [5], [6], [7], [8], [9].

For multistatic/polarimetric systems, the analytical model adopted at the detector design stage has to account for the joint use of all the signals collected from the environment [10], [11], [12] requiring the joint characterization of the signals perceived at the different sensors. Due to the so-called clutter diversity, the inference task becomes challenging since the statistical properties of the disturbance can change among the different nodes and polarizations [13], [14], [15], [16], [17], [18], [19], [20], [21], [22], [23], [24], [25]. In this respect, in [25] a statistical analysis of multistatic/polarimetric sea-clutter returns collected via the netted RADar (NetRAD) system highlighted that, over an appropriate time interval (referred to as the coherence time), the sea-clutter returns collected from both monostatic and bistatic sensors can be modeled according to a spherically invariant random process (SIRP) [26], [27], [28], [29], [30], [31], [32], [33]. This is tantamount to describing the clutter backscattering over the coherence time as the product of a nonnegative random variable and a zero-mean circularly symmetric Gaussian process with unknown spectral characteristics, referred to as texture and speckle, respectively. However, the analyses performed in [25] relied on the use of uncorrelated slow-time samples, and thus no inference on the possible stationarity of the speckle component was made. In this respect, this article represents an important advancement of the study conducted in [25] accounting for possible correlations of the slow-time samples composing the observation vector. Besides, the possible presence of some structures in the clutter covariance matrices (both inter and intra channels) as well as potential relationships between the statistical parameters characterizing the bistatic returns are investigated. This information can be capitalized to design coherent detectors that jointly use all the signals collected from the environment. Precisely, the main innovations of this article are as follows.

1) The design of a test relying on a generalized inner product (GIP) based statistic to assess the stationarity of the data in the slow-time domain.
2) The exploitation of an ad hoc classification technique to explore possible structures within the covariance matrix associated with the speckle component for both monostatic and bistatic measurements.
3) The design of a sequential hypothesis testing procedure to investigate relationships among the covariance matrices of the bistatic data collected over different polarimetric channels and assess their statistical independence.

Although this article focuses on NetRAD data (which, to the best of our knowledge, represents the standard and most extensively studied datasets available in the open literature [10], [11], [12], [13], [14], [15], [16], [17], [18], [19], [20], [21], [22], [23], [24], [25], [34], [35], [36], [37], [38], [39], [40], [41], [42]), it is important to highlight that the developed tests and methodologies are general. They can be applied to make inferences on the interference environment perceived by any coherent multisensor radar system such as multistatic (not necessarily polarimetric) and possibly spatially distributed multiple input–multiple output (MIMO) radars [43], [44] as well as in synthetic aperture radar (SAR) [45], [46], [47], [48]. This represents an important contribution from the theoretical point of view of this study.

The results on the considered real measurements show that the analyzed data can be modeled as drawn from a stationary Gaussian process within the coherence time (as predicted by the SIRP model). Furthermore, the covariance matrix associated with the speckle for the monostatic (bistatic) measurements generally exhibits a centrohermitian (centrosymmetric) structure which is a necessary condition for the observations to be deemed as drawn from a wide sense stationary (WSS) process. This suggests the need for a preclassification procedure to select the most appropriate model for the spectral characteristics of the clutter returns, which is essential to capitalize on the situational awareness at the detector design stage in order to boost target detectability [49], [50], [51]. The study also shows that the bistatic returns on the different polarimetric channels can be modeled as jointly Gaussian and statistically independent within the coherence time, regardless of the sensing system setup. Finally, depending on the transmit/receive polarization and bistatic geometry the speckle components can exhibit proportional/equal covariance matrices, namely they can share the same spectral features. This information can be exploited to force further structure on the analytical model for the received signals. In this respect, by leveraging the considered sequential hypothesis testing it is possible to select the most appropriate signal model depending on the spectral properties of the bistatic measurements.

The remainder of this article is organized as follows. Section II is devoted to a short description of both the NetRAD system and the radar measurements used in this study. In Sections III and IV, the statistical tools designed to assess the stationarity of the data and to identify possible structures of the covariance matrix are discussed for both monostatic and bistatic measurements, respectively. In Section V, the statistical independence of bistatic measurements collected on the different polarimetric channels is studied. Finally, in Section VI, the conclusions are drawn and possible future research avenues are pointed out.

A. Notation

Boldface is used for vectors $\boldsymbol{a}$ (lower case), and matrices $\boldsymbol{A}$ (upper case). The transpose and the conjugate transpose operators are denoted by the symbols $(\cdot)^T$, and $(\cdot)^\dagger$, respectively. $\mathbb{C}^{N\times K}$ is the set of complex-valued vectors with dimension $N \times K$. The curled inequality symbol $\succeq$ (and its strict form $\succ$) is used to denote generalized matrix inequality: for any Hermitian matrix $\boldsymbol{A}$, $\boldsymbol{A} \succeq \boldsymbol{0}$ means that $\boldsymbol{A}$ is a positive semi-definite matrix ($\boldsymbol{A} \succ \boldsymbol{0}$ for positive definiteness). The symbol $\Re\{\boldsymbol{A}\}$ denotes the real part of $\boldsymbol{A} \in \mathbb{C}^{N\times N}$. Finally, $\boldsymbol{x} \sim \mathcal{CN}(\boldsymbol{a}, \boldsymbol{M})$ indicates that $\boldsymbol{x}$ is a complex circular normal vector with mean vector $\boldsymbol{a}$ and covariance matrix $\boldsymbol{M} \succ \boldsymbol{0}$.

II. NetRAD System and Dataset Description

NetRAD is an S-band ground-based multistatic/polarimetric system allowing the simultaneous collection of both monostatic and bistatic radar returns. It was initially developed by the University College London (UCL) and successively modified via a joint collaboration between UCL and the University of Cape Town (UCT), obtaining separate active and passive nodes with baselines in the order of a kilometer. This was achieved by synchronizing the entire system using GPS disciplined oscillators (GPSDOs) at each node, thus avoiding cabled connections (as in the original version of the NetRAD) and granting more degrees of freedom in terms of baselines among nodes [15].

Data exploited in this article were collected on June 9th, 2011 in South Africa at Misty Cliffs using three nodes: one active (with transmit and receive capabilities) and two passive (see [20], [25] for more details). The active node was a pulsed radar operating over a carrier frequency of 2.4 GHz, transmitting linear up-chirp waveforms with a swept bandwidth of 45 MHz (i.e., a range resolution of 3.3 m), and a pulse repetition frequency (PRF) equal to 1 kHz. In addition, the pulse length was ruled so that the cell under test was not eclipsed and the chirp rate was regulated to achieve the aforementioned resolution. The passive receiver nodes were co-located 1830 m away from the active node and used to measure the bistatic sea-clutter returns from both the horizontal and the vertical polarization. As to the geometric configuration, different bistatic angles (β) were considered by pointing the antennas at the active and passive nodes to a common clutter patch so that the intersection point between the boresight of the transmitting/receiving antennas and the position of the nodes occupy the vertices of an isosceles triangle (with axis of symmetry perpendicular to the baseline) [25]. The common clutter patch corresponds to the area where the transmitting and receiving antenna main beams intersect [25]. Fig. 1 shows a pictorial representation of the system geometry for $\beta = 60°$, where N3 (Node 3) is the

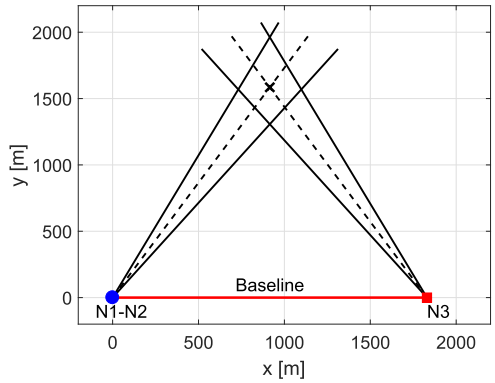

Fig. 1. System geometry for $\beta = 60°$. N3 is the monostatic node, whereas N1-N2 are the two co-located bistatic sensors.

TABLE I
POLARIZATION CONFIGURATIONS FOR THE CONSIDERED MEASUREMENTS

Dataset number	Pol. Node 3 (Tx-Rx)	Pol. Node 1 (Rx)	Pol. Node 2 (Rx)	β [deg]
1	HH	H	V	60
4	HH	H	V	90
5	HH	H	V	95
8	VH	H	V	60
11	VH	H	V	90
12	VH	H	V	95

monostatic node, whereas N1-N2 (Node 1-Node 2) are the two co-located bistatic sensors.[1]

Table I summarizes the polarization configurations and bistatic angles associated with the datasets considered in this study. Therein, the letters H and V denote horizontal and vertical polarization, respectively.

As to the environmental conditions (wind speed/direction and wave height/direction), they remained almost constant during the experiments, with wind speed in the order of 20–28 km/h and wave height in the order of 1.5–2.5 m (corresponding to a sea state 4). For all the acquisition scenarios, measurements refer to a time span of 130 s which, with a PRF of 1 kHz, corresponds to $N_s = 130\,000$ complex-valued slow-time samples for each range cell. In the following, before proceeding with data analysis, the available slow-time measurements are suitably preprocessed so as to remove possible dc offset and imbalance between the quadrature channels [52].

III. STATIONARITY ASSESSMENT

In this section, suitable statistical tools are employed to establish whether the available sea-clutter returns can be modeled as drawn from a stationary Gaussian process. To this end, let us observe that a necessary condition for stationarity is the homogeneity of the sea-clutter measurements over the slow-time dimension (i.e., the data share the same spectral properties). This can be assessed via the GIP, which is a quadratic form commonly used in radar signal processing to assess whether a set of statistically independent zero-mean complex-valued Gaussian random vectors is homogeneous [53], [54], [55]. Precisely, given K independent and identically distributed N-dimensional data vectors $\boldsymbol{x}_k \sim \mathcal{CN}(0, \boldsymbol{\Sigma}) \in \mathbb{C}^{N\times 1}$, $k = 1, \ldots, K \geq N$, the homogeneity property can be established exploiting the following considerations.

1) $\boldsymbol{\Sigma}$ can be estimated according to the maximum likelihood (ML) criterion via the sample covariance matrix (SCM), defined as

$$\hat{\boldsymbol{\Sigma}} = \frac{1}{K}\sum_{k=1}^{K} \boldsymbol{x}_k \boldsymbol{x}_k^{\dagger}. \tag{1}$$

2) The GIP statistics, defined by the following quadratic forms

$$\xi_k = \frac{1}{K}\boldsymbol{x}_k^{\dagger}\hat{\boldsymbol{\Sigma}}^{-1}\boldsymbol{x}_k, \quad k = 1, \ldots, K, \tag{2}$$

follow a complex central Beta-distribution with shape parameters N and $M = K - N$, i.e., $\xi_k \sim \mathcal{CB}_{N,M}$, $k = 1, \ldots, K$.

Leveraging (2), the following proposition follows.

Proposition 1: Let us consider K statistically independent data vectors. A necessary condition for the measurements $\boldsymbol{x}_k \in \mathbb{C}^{N\times 1}$, $k = 1, \ldots, K$, $K \geq N$, to be modeled as homogeneous zero-mean circularly symmetric complex Gaussian random vectors is that the quadratic forms ξ_k, $k = 1, \ldots, K$, are distributed according to a $\mathcal{CB}_{N,K-N}$ model.

Applying this framework to the multistatic/polarimetric data collected from the NetRAD system it is possible to study their homogeneity properties. As a preliminary remark, let us observe that in [25] it has been shown that within the coherence time, both the monostatic and bistatic NetRAD measurements comply with the SIRP model, i.e., within the coherence time they can be deemed as locally Gaussian. Precisely, denoting by $z(t)$ the continuous-time version of the signal collected at the ith sensor, it can be expressed as

$$z(t) = sg(t), \quad t \in T_c \tag{3}$$

where s represents the texture component modeled as a nonnegative random variable over the coherence time, $g(t)$ denotes the speckle component described as a zero-mean circularly symmetric Gaussian process, and T_c is the coherence time. However, the analyses performed in [25] required the use of uncorrelated slow-time samples (practically obtained subsampling the observations) and thus no inference was made on the possible stationarity of the speckle component (due to Gaussianity it is just necessary to study the covariance matrix stationarity as it implies the strict stationarity of the process).

In the following, the study conducted in [25] is completed accounting for possible correlations of the slow-time samples composing the observation vector. To this end, let us denote by

$$\{\boldsymbol{z}_{i,k}\}_{k=1}^{K}, \quad i = 1, 2, 3$$

a set of K data vectors containing N consecutive slow-time samples collected from a given range cell at the ith node. To ensure uncorrelation and statistical independence of the data vectors $\boldsymbol{z}_{i,k}$, $k = 1, \ldots, K$, $i = 1, 2, 3$, they are spaced in the slow-time domain according to the average decorrelation time of 0.05 s [25] which, at PRF of 1 kHz, corresponds

[1]Given the co-location and synchronization of the passive nodes using GPSDOs, they can be considered (for the receive chain) as a single node equipped with two coherent polarimetric channels.

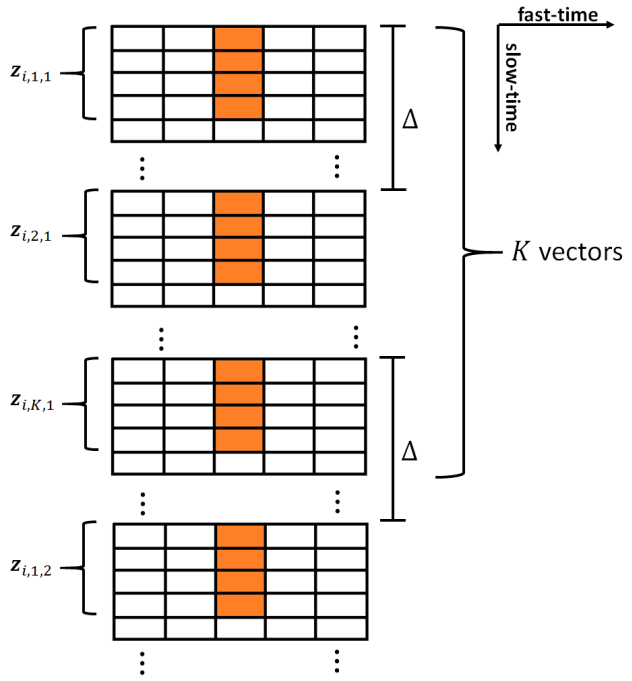

Fig. 2. Pictorial representation of the data selection procedure.

to a minimum temporal lag between two observation vectors of $\Delta = 50$ samples. Precisely, denoting by $z_i \in \mathbb{C}^{N_s \times 1}$ the available measurements in the slow-time dimension acquired at the ith sensor, the set of K data vectors can be selected as follows:

$$z_{i,k,l} = \left[z_i\left(\Delta_{k,l}+1\right), \ldots, z_i\left(\Delta_{k,l}+N\right)\right]^T \in \mathbb{C}^{N\times 1} \tag{4}$$

$k = 1, \ldots, K$, $l = 1, 2, \ldots, L$, where:

1) the index l allows the selection of L different groups of K data vectors from the available N_s slow-time samples, that is,
$$L = \left\lfloor \frac{N_s - N + \Delta}{K\Delta} \right\rfloor$$
2) for a given (k, l)-pair, $\Delta_{k,l} = [(l-1)K + k - 1]\Delta$, allows the selection of the kth N-dimensional data vector for the lth data selection; and
3) $(K\Delta/\mathrm{PRF}) < T_c$, i.e., each group of K data vectors are picked up within the coherence time.

Fig. 2 shows a pictorial representation of the data selection procedure with reference to the first set of K data vectors, i.e., considering $l = 1$.

Using this data selection procedure, for a given range cell the GIP statistics can be computed according to Algorithm 1. Thus, relying on Proposition 1 the homogeneity of the data can be studied by comparing the cumulative distribution function (CDF) of a $\mathcal{CB}_{N,M}$ random variable with the empirical CDF (ECDF) of the GIP statistics. This analysis can be conducted via a visual comparison between the theoretical and the actual CDFs, and/or by testing the simple hypotheses

$$H_0^{(i,k)} : \xi_{i,k} \text{ has the CDF } F_X \tag{5}$$

$k = 1, \ldots, K$, $i = 1, 2, 3$, with F_X denoting the CDF of the random variable $X \sim \mathcal{CB}_{N,M}$. In Sections III-A and III-B, both studies are performed considering the datasets 1, 4, 5, 8, 11, and 12, and assuming $N = 8$ and $K = 2N$.

Algorithm 1 Procedure to Compute the GIP Statistics for a Given Range Cell

Input: $z_{i,k,l}$, $i = 1, 2, 3$, $k = 1, \ldots, K$, $l = 1, \ldots, L$;
Output: GIP statistics for a given range cell;
1: set $l = 0$;
2: **repeat**
3: set $l = l + 1$;
4: compute the SCM
$$\hat{\boldsymbol{\Sigma}}_{i,l} = \frac{1}{K}\sum_{k=1}^{K} z_{i,k,l} z_{i,k,l}^{\dagger}, \quad i = 1, 2, 3$$
5: compute the quadratic forms
$$\xi_{i,k,l} = \frac{1}{K} z_{i,k,l}^{\dagger} \hat{\boldsymbol{\Sigma}}_{i,l}^{-1} z_{i,k,l}, \quad i = 1, 2, 3, \quad k = 1, \ldots, K$$
6: **until** $l \leq L$

A. Analysis Based on CV Distance

The aim of this analysis is to visually compare the theoretical and the empirical CDF of the GIP statistics. To this end, for a given sensor/range cell pair, the ECDF is computed starting from the samples

$$\boldsymbol{\xi}_i^{CV} = \left[\boldsymbol{\xi}_{i,1}^{CV}, \ldots, \boldsymbol{\xi}_{i,L}^{CV}\right], \quad i = 1, 2, 3 \tag{6}$$

where

$$\boldsymbol{\xi}_{i,l}^{CV} = \left[\xi_{i,1,l}, \ldots, \xi_{i,K,l}\right], \quad l = 1, \ldots, L, \quad i = 1, 2, 3\,. \tag{7}$$

Fig. 3 displays the ECDFs corresponding to each range cell of the clutter patch and sensor together with the theoretical CDF. By visual inspection of the curves it is possible to establish that:

1) regardless of the considered dataset/range cell, the ECDF associated with the bistatic measurements achieves a good agreement with the theoretical model;
2) the ECDF corresponding to the horizontally co-polarized bistatic measurements are closer than the monostatic counterparts to the theoretical model [see Fig. 3(a), (c), and (d)].

The latter consideration can be further corroborated by the means of the Cramer Von Mises (CV) distance. This is an integral-based distributional distance between two CDFs and given a set of L identically distributed observations $[X_1, \ldots, X_L]$ of the random variable X, its formal definition is given by

$$d_{\mathrm{CV}} = \frac{1}{12L} + \sum_{l=1}^{L}\left| F_X\left(X_{(l)}\right) - \frac{2l-1}{2L}\right|^2 \tag{8}$$

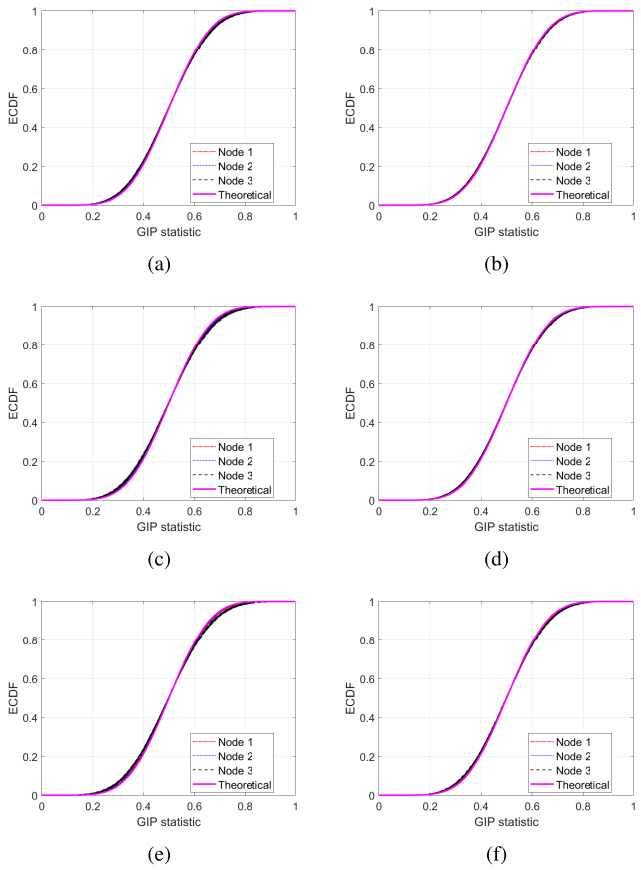

Fig. 3. ECDFs evaluated using the GIP statistics for the three nodes: (a) dataset 1, (b) dataset 8, (c) dataset 4, (d) dataset 11, (e) dataset 5, and (f) dataset 12.

TABLE II
AVERAGE CV DISTANCE

Dataset	Node 1	Node 2	Node 3
1	0.14	0.09	1.28
8	0.08	0.09	0.29
4	0.19	0.24	2.81
11	0.11	0.11	0.67
5	0.24	0.11	3.97
12	0.11	0.24	0.87

where $F_X(\cdot)$ is the CDF of the assumed distribution and $X_{(l)}$ is the lth order statistic from the set of random variables. Using this metric, with reference to each dataset, Table II reports the mean CV distance obtained by averaging the values of d_{CV} computed for each range cell of the clutter patch. The values confirm that for the horizontally co-polarized case (datasets 1, 4, and 5), the mean CV distance for the monostatic measurements is higher than the bistatic counterpart. Interestingly, for this configuration, it is also possible to observe that the CV index increases as the distance between the monostatic node and the clutter patch reduces. Specifically, since for the NetRAD system the position of the nodes is fixed, the distance between the sensors and the clutter patch reduces as the bistatic angle increases.

B. Analysis via Hypothesis Testing

The aim of this analysis is to verify whether the GIP statistics follow a $\mathcal{CB}_{N,M}$ model by testing the simple hypotheses in (5). The study is conducted by using the Kolmogorov–Smirnov (KS) test, a nonparametric statistical method designed to assess the goodness-of-fit between an empirical and a theoretical distribution function [56]. It is based on the maximum absolute difference between the empirical and the hypothesized CDFs of the data, known as the KS statistic. Notably, the limiting (asymptotic) distribution of the KS statistic under the null hypothesis is known and parameter-free. Consequently, for a given significance level, the threshold used to evaluate the conformity of the data to the hypothesized statistical model can be assumed independent of the tested distribution.

TABLE III
PERCENTAGE OF GIP STATISTICS FOR WHICH THE BETA DISTRIBUTION CANNOT BE REJECTED FOR A 0.01 SIGNIFICANCE LEVEL

Dataset	Node 1	Node 2	Node 3
1	99.1	98.9	98.3
8	99.0	99.0	98.8
4	98.8	98.9	97.5
11	98.9	99.0	98.5
5	98.9	99.0	97.8
12	99.0	98.9	98.7

For a given range cell the KS statistic in (5) is computed using the samples

$$\boldsymbol{\xi}_{i,k}^{\mathrm{KS}} = \left[\xi_{i,k,1}, \ldots, \xi_{i,k,L}\right], \quad i = 1, 2, 3, \ k = 1, \ldots, K\,. \tag{9}$$

Applying the KS test to the considered problem, Table III shows the average percentage of GIP statistics for which the $\mathcal{CB}_{N,M}$ distribution cannot be rejected for a 0.01 significance level. Precisely, for each sensor and a given range cell, the samples $\boldsymbol{\xi}_{i,k}^{\mathrm{KS}}$, $i = 1, 2, 3$, $k = 1, \ldots, K$, are used to perform K different KS test. Then, the results are averaged with respect to both the number of data vectors and range cells. Results pinpoint that within the coherence time, the considered measurements can be deemed as homogeneous (i.e., compatible with stationarity) and locally Gaussian (as predicted by the SIRP model). In other words, within the coherence time for both the monostatic and bistatic sensors the received data can be modeled as a zero-mean circularly symmetric complex Gaussian random vector with a specific covariance matrix, which can be possibly different from one sensor to another as well as along the range domain or in different coherence time intervals.

IV. COVARIANCE MATRIX SYMMETRY IDENTIFICATION

The analysis in Section III highlighted that the available multistatic/polarimetric measurements can be considered as drawn from a stationary Gaussian process within the coherence time. However, no inferences can be made over a time scale greater than the coherence time or about the spectral features of the sea-clutter perceived at different sensors or polarizations. In this respect, some insights can be gained by studying the symmetries of the covariance matrix of the speckle component over successive coherence time intervals. Indeed, for a given sensor/range cell a necessary condition for the data observed over different coherence time intervals to share similar spectral characteristics (up to a scale factor

representing the texture component) is that the covariance matrix of the corresponding speckle components exhibit the same structure. Moreover, specific models such as Hermitian unstructured, symmetric unstructured, centrohermitian, and centrosymmetric, can provide information about the spectral behavior of the clutter perceived at different sensors. As a matter of fact, centrosymmetry or centrohermitianity are necessary conditions for the observations to be drawn from a WSS process. Furthermore, for a symmetric or a centrosymmetric structure the spectrum of the clutter has to exhibit a symmetric behavior with respect to the zero-Doppler frequency. For instance, by describing the sea-clutter spectrum with the well-established Gaussian-shaped model, the generic (r, c) entry of the covariance matrix of the speckle component over a coherence time interval can be expressed as

$$\boldsymbol{M}(r,c) = \alpha \rho^{(r-c)^2} e^{j2\pi(r-c)f_d}, \quad (r,c) \in \{1,\ldots,N\}^2 \tag{10}$$

where N is the number of pulses in the coherent processing interval, α is a real-valued positive parameter accounting for the actual texture power, ρ is the one-lag correlation coefficient, and f_d represents the normalized Doppler frequency of the sea-clutter. Thus, a real-valued covariance matrix (symmetric unstructured/centrosymmetric) can be associated to observations with a zero-Doppler frequency. Conversely, complex-valued covariance matrices (Hermitian/centrohermitian) are representative of clutter returns with a nonzero-Doppler frequency.

Based on the previous considerations, the aim of this section is to infer on the structure of the covariance matrix of the speckle component for both the monostatic and the bistatic sea-clutter measurements. To this end, relying on the framework proposed in [57], for a given sensor/range cell and exploiting observations from a specific coherence time interval, covariance symmetries can be studied considering the following hypotheses test:

$$\begin{cases} H_1 : \boldsymbol{M} \in \mathbb{C}^{N\times N}, & \text{is Hermitian unstructured} \\ H_2 : \boldsymbol{M} \in \mathbb{R}^{N\times N}, & \text{is symmetric unstructured} \\ H_3 : \boldsymbol{M} \in \mathbb{C}^{N\times N}, & \text{is centrohermitian} \\ H_4 : \boldsymbol{M} \in \mathbb{R}^{N\times N}, & \text{is centrosymmetric} \end{cases} \tag{11}$$

where the number of unknown parameters under each hypothesis is given by

$$\begin{cases} m_1 = N^2, & \text{under } H_1 \\ m_2 = N(N+1)/2, & \text{under } H_2 \\ m_3 = N(N+1)/2, & \text{under } H_3 \\ m_4 = \begin{cases} \dfrac{N}{2}\left(\dfrac{N}{2}+1\right), & \text{if } N \text{ is even} \\ \left(\dfrac{N+1}{2}\right)^2, & \text{if } N \text{ is odd} \end{cases} & \text{under } H_4. \end{cases} \tag{12}$$

To screen among the different hypotheses, suitable strategies can be exploited which involve the log-likelihood function of the observations, an estimate of the covariance matrix under each hypothesis, and a model order selection (MOS) rule [57]. In this respect, since the analyses are performed within the coherence time the observations can be modeled according to a zero-mean circularly symmetric complex Gaussian model. Besides, assuming the availability of $K \geq N$ independent data vectors $\boldsymbol{Z} = [z_1, \ldots, z_K] \in \mathbb{C}^{N\times K}$, under the ith hypothesis the ML estimate of the covariance matrix of the speckle component is given by

$$\begin{cases} \hat{\boldsymbol{M}}_1 = \dfrac{1}{K}\boldsymbol{Z}\boldsymbol{Z}^\dagger, & (\text{Under } H_1) \\ \hat{\boldsymbol{M}}_2 = \dfrac{1}{K}\Re\{\boldsymbol{Z}\boldsymbol{Z}^\dagger\}, & (\text{Under } H_2) \\ \hat{\boldsymbol{M}}_3 = \dfrac{1}{2K}\left[\boldsymbol{Z}\boldsymbol{Z}^\dagger + \boldsymbol{J}\left(\boldsymbol{Z}\boldsymbol{Z}^\dagger\right)^*\boldsymbol{J}\right], & (\text{Under } H_3) \\ \hat{\boldsymbol{M}}_4 = \dfrac{1}{2K}\Re\{\boldsymbol{Z}\boldsymbol{Z}^\dagger + \boldsymbol{J}\left(\boldsymbol{Z}\boldsymbol{Z}^\dagger\right)^*\boldsymbol{J}\}, & (\text{Under } H_4) \end{cases} \tag{13}$$

where $\boldsymbol{J} \in \mathbb{R}^{N\times N}$ is a permutation matrix such that $\boldsymbol{J}(r,c) = 1$ if and only if $r + c = N + 1$, $(r,c) \in \{1,\ldots,N\}^2$. Finally, as to the classification rule, the Bayesian information criterion (BIC) is used [57]. This is tantamount to considering the decision rule

$$H_{\hat{i}} = \arg\min_{i\in\mathcal{H}}\left\{-2s\left(\hat{\boldsymbol{M}}_i, H_i\right) + m_i \log(K)\right\} \tag{14}$$

where $\mathcal{H} = \{1,2,3,4\}$, whereas $s(\hat{\boldsymbol{M}}_i, H_i)$ and $\hat{\boldsymbol{M}}_i$ are the log-likelihood function and the ML estimate of $\boldsymbol{M}_i$ under the ith hypothesis, respectively.

The analysis is conducted using the data selection procedure specified in (4) for the measurements from datasets 1, 4, 5, 8, 11, 12, assuming $N = 8$ and $K = 2N$. Specifically, for a given sensor, different classification instances are made along the slow-time dimension for each range cell of the clutter patch.

Figs. 4, 6, and 8 display the classified structures for the datasets 1–8, 4–11, and 5–12, respectively. For each range bin of the clutter patch (reported over the horizontal axis of the map), the data selection procedure is applied over the slow-time dimension, providing different classification instances (reported over the vertical axis of the map). For the interpretation of the results, Figs. 5, 7, and 9 show the modulus of the available sea-clutter fast-time/slow-time data for each node and sensing system configuration. The maps highlight that:

1) for both monostatic and bistatic data the top-rated structures are centrohermitian and centrosymmetric (i.e., hypothesis H_3 and H_4, respectively);
2) the monostatic (bistatic) returns generally exhibit a centrohermitian (centrosymmetric) covariance matrix;
3) the number of data classified under H_3 and H_4 (for both monostatic and bistatic measurements) depends upon polarimetric/geometric configuration; and
4) centrosymmetry and centrohermitianity can be linked to the sea-wave profile (which depends on the sea-state).

The latter finding can be identified by comparing Figs. 4 and 5 for datasets 1–8, Figs. 6 and 7 for datasets 4–11, and Figs. 8 and 9 for datasets 5–12.

The aforementioned trends are also corroborated by the percentage of data classified under the hypothesis H_i, $i = 1, 2, 3, 4$ (averaged over the range bins belonging to the clutter patch) presented in Table IV.

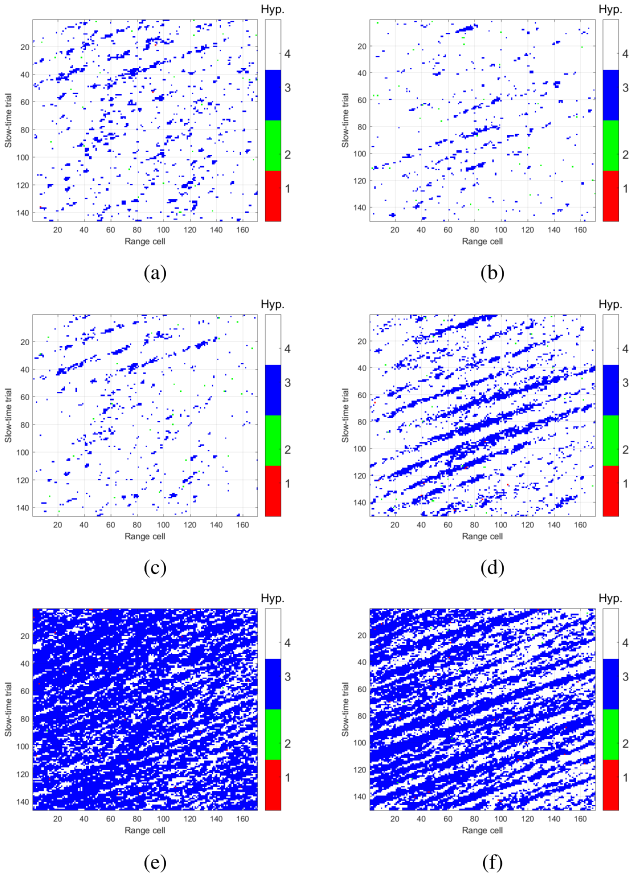

Fig. 4. Structures of the covariance matrix classified using datasets 1 and 8. (a), (c), and (e) Related to dataset 1 nodes 1–3, respectively. (b), (d), and (f) Related to dataset 8 nodes 1–3, respectively.

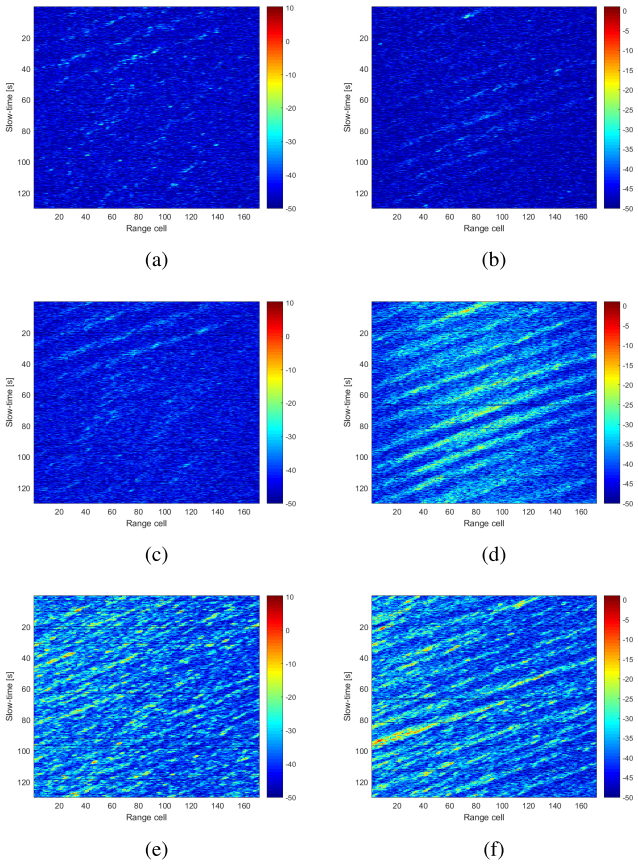

Fig. 5. Modulus (in dB) of the available measurements from datasets 1 and 8. (a), (c), and (e) Related to dataset 1 nodes 1–3, respectively. (b), (d), and (f) Related to dataset 8 nodes 1–3, respectively.

With reference to the bistatic measurements, the obtained values also suggest that when the transmitter is horizontally polarized (datasets 1, 4, and 5), as the bistatic angle increases the percentage of data classified as centrohermitian increases while that identified as centrosymmetric reduces. For the vertically polarized counterpart, this behavior is limited to datasets 8 and 11 (i.e., up to bistatic angles less than or equal to 90°). In addition, for a specific geometric configuration (i.e., datasets 1–8, 4–11, and 5–12), the percentage of data classified under the centrohermitian (centrosymmetric) hypothesis for co-polarized monostatic measurements is higher (smaller) than the value obtained for the cross-polarized counterparts.

Finally, Fig. 10 shows the box and whisker plots of the spectral centroids computed using the data classified under the centrohermitian and centrosymmetric hypothesis. For each range bin, the covariance matrices estimated using the instances classified under H_3 and H_4 are averaged and used to estimate the power spectrum via Capons' method under both hypotheses. Then, the spectral centroids of the resulting power spectra (computed separately for each hypothesis and range bin of the clutter patch) are used to construct the box and whisker plots of Fig. 10. Precisely, for each dataset/node and range cell, the spectral centroid is defined as

$$\left(\sum_{p=1}^{P} P_p f_p\right) \Big/ \left(\sum_{p=1}^{P} P_p\right) \tag{15}$$

TABLE IV
PERCENTAGE OF DATA CLASSIFIED UNDER EACH HYPOTHESIS

Dataset	Node	H_1	H_2	H_3	H_4
1	1	0.01	0.12	6.58	93.29
	2	0.00	0.12	3.91	95.98
	3	0.13	0.02	75.82	24.03
8	1	0.00	0.12	3.07	96.81
	2	0.04	0.13	16.85	82.98
	3	0.11	0.06	57.06	42.78
4	1	0.02	0.09	15.91	83.98
	2	0.10	0.14	17.95	81.82
	3	0.84	0.01	95.57	3.58
11	1	0.02	0.14	10.86	88.97
	2	0.07	0.08	35.53	64.32
	3	0.27	0.01	91.25	8.47
5	1	0.04	0.14	21.56	78.25
	2	0.08	0.08	25.45	74.40
	3	0.81	0.07	96.60	2.52
12	1	0.03	0.10	10.14	89.74
	2	0.06	0.04	33.41	66.49
	3	0.14	0.00	94.21	5.65

where P is the total number of considered Doppler bins, whereas f_p and P_p are the values of the frequency and the power spectrum corresponding to the pth Doppler bin, respectively.

Regardless of the measurement setup, the plots show that:

1) the spectral centroids associated with the monostatic data are higher than those of the bistatic counterpart;

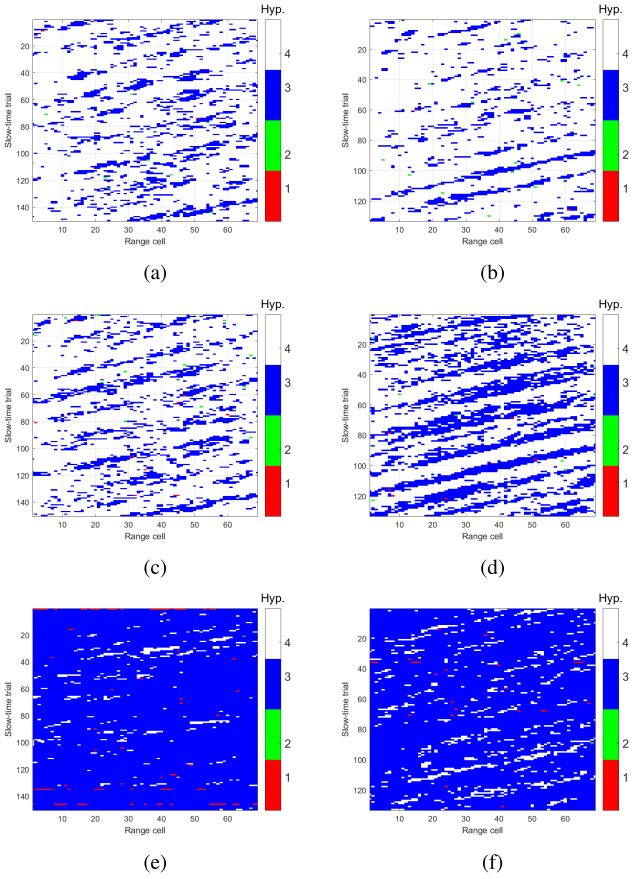

Fig. 6. Structures of the covariance matrix classified using datasets 4 and 11. (a), (c), and (e) Related to dataset 4 nodes 1–3, respectively. (b), (d), and (f) Related to dataset 11 nodes 1–3, respectively.

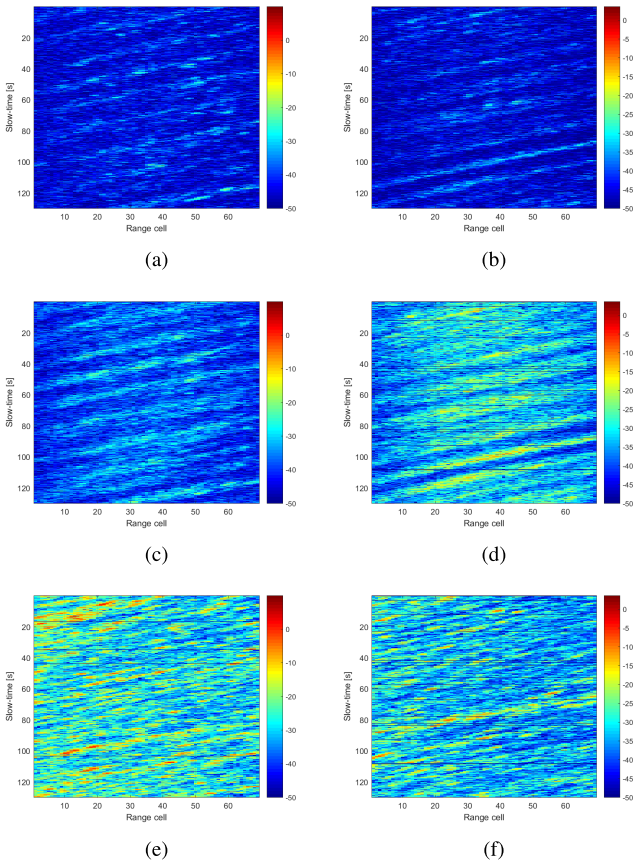

Fig. 7. Modulus (in dB) of the available measurements from datasets 4 and 11. (a), (c), and (e) Related to dataset 4 nodes 1–3, respectively. (b), (d), and (f) Related to dataset 11 nodes 1–3, respectively.

TABLE V

MEDIAN VALUE OF THE SPECTRAL CENTROIDS (IN HZ) OBTAINED FOR EACH SENSOR UNDER THE HYPOTHESES H_3 AND H_4

	Node 1		Node 2		Node 3	
Dataset	H_3	H_4	H_3	H_4	H_3	H_4
1	17	3	15	4	38	11
4	15	5	13	6	47	17
5	17	5	14	7	49	17
8	15	2	14	6	34	10
11	15	5	13	7	40	14
12	14	5	11	6	41	15

2) the spectral centroids obtained under H_4 are smaller than those under H_3; and
3) for a specific hypothesis, the spectral centroids of the cross-polarized bistatic measurements are almost the same.

The aforementioned trends can be also corroborated by the median values of the spectral centroids reported in Table V.

Summarizing, the main findings of this analysis confirm that over a time scale greater than the coherence time, the sea-clutter returns collected at the active and passive sensors cannot be modeled as drawn from a stationary process. Indeed, for each range cell, both the structure of the covariance matrix and the spectral features of the data can change along the slow-time dimension. However, within the coherence time, the data generally exhibit a centrohermitian/centrosymmetric covariance matrix, further corroborating the presence of an underlying WSS process. Moreover, the results highlight that the structure/symmetries of the covariance matrix depend upon the polarimetric/geometric configuration of the sensing system and the sea-wave profile as well. Therefore, the analysis suggests the use of a preclassification procedure of the data at both monostatic and bistatic sides to select the most appropriate model for the covariance functional form which can be capitalized by radar signal processing schemes. Finally, the analysis of the spectral centroids suggests that for a specific hypothesis, the cross-polarized bistatic measurements exhibit similar values of this feature. This information is of paramount importance to develop detection schemes leveraging cross-polarized bistatic measurements and is further investigated in Section V.

V. STATISTICAL INDEPENDENCE OF THE BISTATIC MEASUREMENTS

In this section, a sequential hypothesis testing procedure is developed to assess whether the cross-polarized bistatic measurements can be deemed statistically independent and whether they share the same spectral properties.

In this respect, based on the analysis performed in Section III, within the coherence time the cross-polarized bistatic measurements can be modeled as zero-mean circularly symmetric complex Gaussian vectors. Thus, for a specific range cell, denoting by $\boldsymbol{z}_i \in \mathbb{C}^{N\times 1}$ a vector containing N

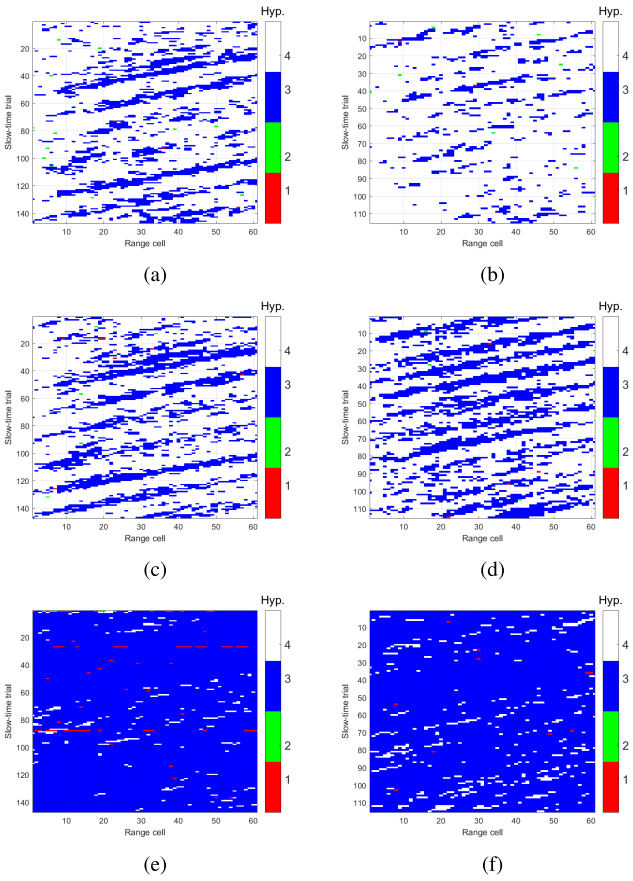

Fig. 8. Structures of the covariance matrix classified using datasets 5 and 12. (a), (c), and (e) Related to dataset 5 nodes 1–3, respectively. (b), (d), and (f) Related to dataset 12 nodes 1–3, respectively.

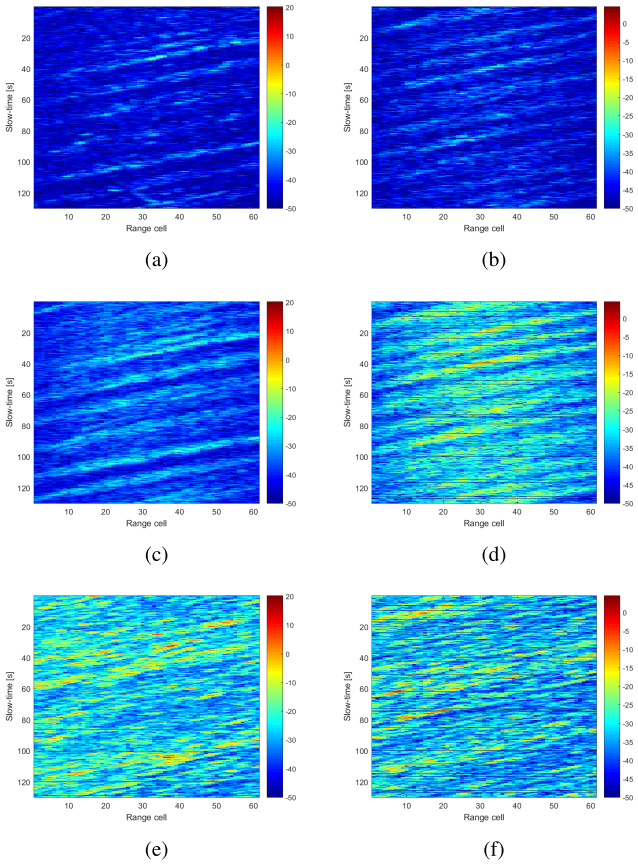

Fig. 9. Modulus (in dB) of the available measurements from datasets 5 and 12. (a), (c), and (e) Related to dataset 5 nodes 1–3, respectively. (b), (d), and (f) Related to dataset 12 nodes 1–3, respectively.

consecutive slow-time samples collected within the coherence time using the ith bistatic node, this vector can be modeled as $\boldsymbol{z}_i \sim \mathcal{CN}(0, \boldsymbol{M}_i)$, $i = 1, 2$. With this preliminary remark, the focus of this section is to assess whether the following conditions hold:

1) $\boldsymbol{z}_1$ and $\boldsymbol{z}_2$ are statistically independent;
2) $\boldsymbol{z}_1$ and $\boldsymbol{z}_2$ are statistically independent with proportional covariance matrix, i.e., $\boldsymbol{M}_2 = \gamma \boldsymbol{M}_1$, $\gamma \in \mathbb{R}^+$; and
3) $\boldsymbol{z}_1$ and $\boldsymbol{z}_2$ are statistically independent and share the same covariance matrix, i.e., $\boldsymbol{M}_1 = \boldsymbol{M}_2 = \boldsymbol{M}$.

To this end, let us assume that the data vector $\boldsymbol{z} = [\boldsymbol{z}_1^T \, \boldsymbol{z}_2^T]^T \in \mathbb{C}^{2N \times 1}$ formed by stacking the cross-polarized bistatic measurements is a zero-mean circularly symmetric complex Gaussian vector, with covariance matrix

$$\boldsymbol{\Sigma} = \mathbb{E}\left[\boldsymbol{z}\boldsymbol{z}^{\dagger}\right] = \begin{bmatrix} \boldsymbol{M}_1 & \boldsymbol{M}_{12} \\ \boldsymbol{M}_{12}^{\dagger} & \boldsymbol{M}_2 \end{bmatrix} \tag{16}$$

where $\boldsymbol{M}_{12} = \mathbb{E}[\boldsymbol{z}_1 \boldsymbol{z}_2^{\dagger}]$. Hence, conditions 1–3, can be assessed by analyzing the characteristics of $\boldsymbol{\Sigma}$. Indeed:

1) under condition 1, $\boldsymbol{\Sigma} = \mathbf{Diag}\,(\boldsymbol{M}_1, \boldsymbol{M}_2)$;
2) under condition 2, $\boldsymbol{\Sigma} = \mathbf{Diag}\,(\boldsymbol{M}_1, \gamma \boldsymbol{M}_1)$; and
3) under condition 3, $\boldsymbol{\Sigma} = \mathbf{Diag}\,(\boldsymbol{M}, \boldsymbol{M})$.

Formally, letting

$$\Theta_0 = \left\{\boldsymbol{\Sigma} \in \mathbb{H}^{2N \times 2N} : \boldsymbol{\Sigma} \succ 0\right\}$$
$$\Theta_1 = \left\{\boldsymbol{\Sigma} \in \mathbb{H}^{2N \times 2N} : \boldsymbol{\Sigma} \succ 0, \ \boldsymbol{\Sigma} = \mathbf{Diag}\,(\boldsymbol{M}_1, \boldsymbol{M}_2)\right\}$$
$$\Theta_2 = \left\{\boldsymbol{\Sigma} \in \mathbb{H}^{2N \times 2N} : \boldsymbol{\Sigma} \succ 0, \ \boldsymbol{\Sigma} = \mathbf{Diag}\,(\boldsymbol{M}, \gamma \boldsymbol{M})\right\}$$
$$\Theta_3 = \left\{\boldsymbol{\Sigma} \in \mathbb{H}^{2N \times 2N} : \boldsymbol{\Sigma} \succ 0, \ \boldsymbol{\Sigma} = \mathbf{Diag}\,(\boldsymbol{M}, \boldsymbol{M})\right\} \tag{17}$$

the problem at hand can be stated in terms of the following hypothesis test:

$$\begin{cases} H_0 : \boldsymbol{\Sigma} \in \Theta_0 \\ H_1 : \boldsymbol{\Sigma} \in \Theta_1 \\ H_2 : \boldsymbol{\Sigma} \in \Theta_2 \\ H_3 : \boldsymbol{\Sigma} \in \Theta_3. \end{cases} \tag{18}$$

Since $\Theta_3 \subseteq \Theta_2 \subseteq \Theta_1 \subseteq \Theta_0$, the hypotheses in (18) are nested. Hence, to discriminate among them, the tailored sequential hypothesis testing procedure of (19), as shown at the bottom of page 11 is considered. Specifically, the test T_1 is first used to verify whether condition 1 holds. Then, condition 2 is tested via T_2 only for the data that satisfies H_{01}, and finally, condition 3 is tested via T_3 for the data complying with both H_{01} and H_{02}.

The hypothesis tests T_1, T_2, and T_3, can be handled via the generalized likelihood ratio (GLR) criterion, which is tantamount to replacing in the likelihood ratio test (LRT) the unknown parameters under each hypothesis with their respective ML estimates. Leveraging this framework, it is possible to show that the GLR test (GLRT) for T_1, T_2, and

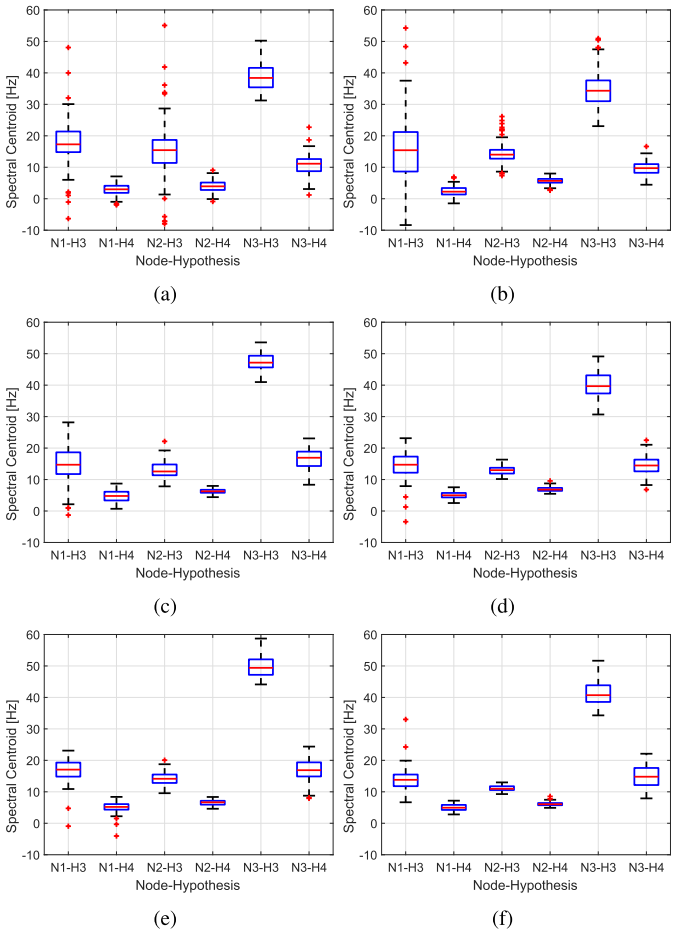

Fig. 10. Box and whisker plots of the spectral centroids under hypothesis H_3 and H_4 for the three nodes: (a) dataset 1, (b) dataset 8, (c) dataset 4, (d) dataset 11, (e) dataset 5, and (f) dataset 12.

T_3, can be written as [58], [59], [60]

$$\frac{\det\left[\mathbf{Diag}\left(\boldsymbol{S}_1, \boldsymbol{S}_2\right)\right]}{\det(\boldsymbol{S})} \underset{H_0}{\overset{H_1}{\gtrless}} \eta_1 \quad \text{(for test } T_1\text{)} \tag{20}$$

$$\hat{\gamma}_1{}^N \frac{\det^2\left(\frac{\boldsymbol{S}_1}{\hat{\gamma}_1} + \boldsymbol{S}_2\right)}{\det(\boldsymbol{S}_1)\det(\boldsymbol{S}_2)} \underset{H_0}{\overset{H_1}{\gtrless}} \eta_2 \quad \text{(for test } T_2\text{)} \tag{21}$$

$$\frac{\det^2\left(\frac{\boldsymbol{S}_1 + \boldsymbol{S}_2}{2K}\right)}{\det^2(\hat{\boldsymbol{R}}_1)\hat{\gamma}_2^N} \underset{H_0}{\overset{H_1}{\gtrless}} \eta_3 \quad \text{(for test } T_3\text{)} \tag{22}$$

where:

1) η_1, η_2, and η_3, are the decision thresholds for a given false alarm probability (P_{fa});
2) $\boldsymbol{S} = \boldsymbol{Z}\boldsymbol{Z}^{\dagger}$, with $\boldsymbol{Z} = [\boldsymbol{Z}_1^T\ \boldsymbol{Z}_2^T]^T \in \mathbb{C}^{N\times 2K}$, $N \geq 2K$, in which $\boldsymbol{Z}_i \in \mathbb{C}^{N\times K}$, is a data matrix of K statistically independent homogeneous data vectors whose entries are N consecutive slow-time samples collected at the ith sensor for a specific range cell, $i = 1, 2$;
3) $\boldsymbol{S}_i = \boldsymbol{Z}_i\boldsymbol{Z}_i^{\dagger}$, $i = 1, 2$;
4) parameter $\hat{\gamma}_1$ in (21) is computed via the iterative procedure specified in Algorithm 2; and
5) parameters $\hat{\gamma}_2$ and $\hat{\boldsymbol{R}}_1$ in (22) are obtained via the iterative procedure described in Algorithm 3.

Algorithm 2 Procedure to Compute γ_1

Input: $\boldsymbol{S}_1$, $\boldsymbol{S}_2$, N, K, Q_1
Output: an estimate of γ_1

set $q = 1$, $\boldsymbol{B}_q = \boldsymbol{I}$
repeat
  $q = q + 1$
  $\alpha_q = \dfrac{\mathrm{tr}\left(\boldsymbol{S}_1\boldsymbol{B}_{q-1}^{-1}\right)}{KN}$
  $\boldsymbol{B}_q = \dfrac{1}{2K}\left(\dfrac{\boldsymbol{S}_1}{\alpha_q} + \boldsymbol{S}_2\right)$
until $q \leq Q_1$
set $\hat{\gamma}_1 = \alpha_q$

Algorithm 3 Procedure to Compute $\hat{\gamma}_2$ and $\hat{\boldsymbol{R}}_1$

Input: $\boldsymbol{S}_1$, $\boldsymbol{S}_2$, N, K, Q_2
Output: $\hat{\gamma}_2$, $\hat{\boldsymbol{R}}_1$

set $q = 1$, $\boldsymbol{B}_q = \boldsymbol{I}$
repeat
  $q = q + 1$
  $\alpha_q = \dfrac{\mathrm{tr}\left(\boldsymbol{S}_2\boldsymbol{B}_{q-1}^{-1}\right)}{KN}$
  $\boldsymbol{B}_q = \dfrac{1}{2K}\left(\boldsymbol{S}_1 + \dfrac{\boldsymbol{S}_2}{\alpha_q}\right)$
until $q \leq Q_2$
set $\hat{\gamma}_2 = \alpha_q$ and $\hat{\boldsymbol{R}}_1 = \boldsymbol{B}_q$

Remarkably, invoking the convergence properties of alternating optimization, any limit point resulting from Algorithm 2 (3) is a stationary point to the ML estimation problem under the assumption $\boldsymbol{\Sigma} \in \Theta_2$ [61]. Nevertheless, leveraging the geodically convexity of the negative-log-likelihood function with respect to $\boldsymbol{M}$ and γ [62], it is not difficult to show that the sequence generated by Algorithm 3 converges to the ML estimate. In addition, the considered detectors ensure the constant false alarm rate property with respect to the unknowns. In fact, the statistical characterization of the decision statistic:

1) in (20) does not depend on the nuisance parameter under H_{01}, i.e., $\boldsymbol{\Sigma}$, owing on the properties of the det-function;
2) in (21) does not depend on the nuisance parameters under H_{02}, i.e., $\boldsymbol{\Sigma}$ and γ, due to the properties of the det-function as well as the scale invariance of the γ estimate provided by Algorithm 2; and
3) in (22) does not depend on the nuisance parameters under H_{03}, i.e., $\boldsymbol{\Sigma}$ and γ, due to the properties of the det-function as well as the joint scale invariance of the γ factor and $\boldsymbol{\Sigma}$ estimates.

In order to apply the developed statistical tools, the foregoing analysis is conducted using the same data selection procedure and system parameters as in Section IV, i.e., $N = 8$, and $K = 2N$. The number of iterations for Algorithms 2 and 3 is set to 20 ($Q_1 = Q_2 = 20$), and the detection thresholds are set to ensure $P_{fa} = 10^{-2}$ assuming zero-mean complex circular white Gaussian data.

Figs. 11–13 show the detection maps obtained using datasets 1–8, 4–11, and 5–12, respectively. As mentioned before, the

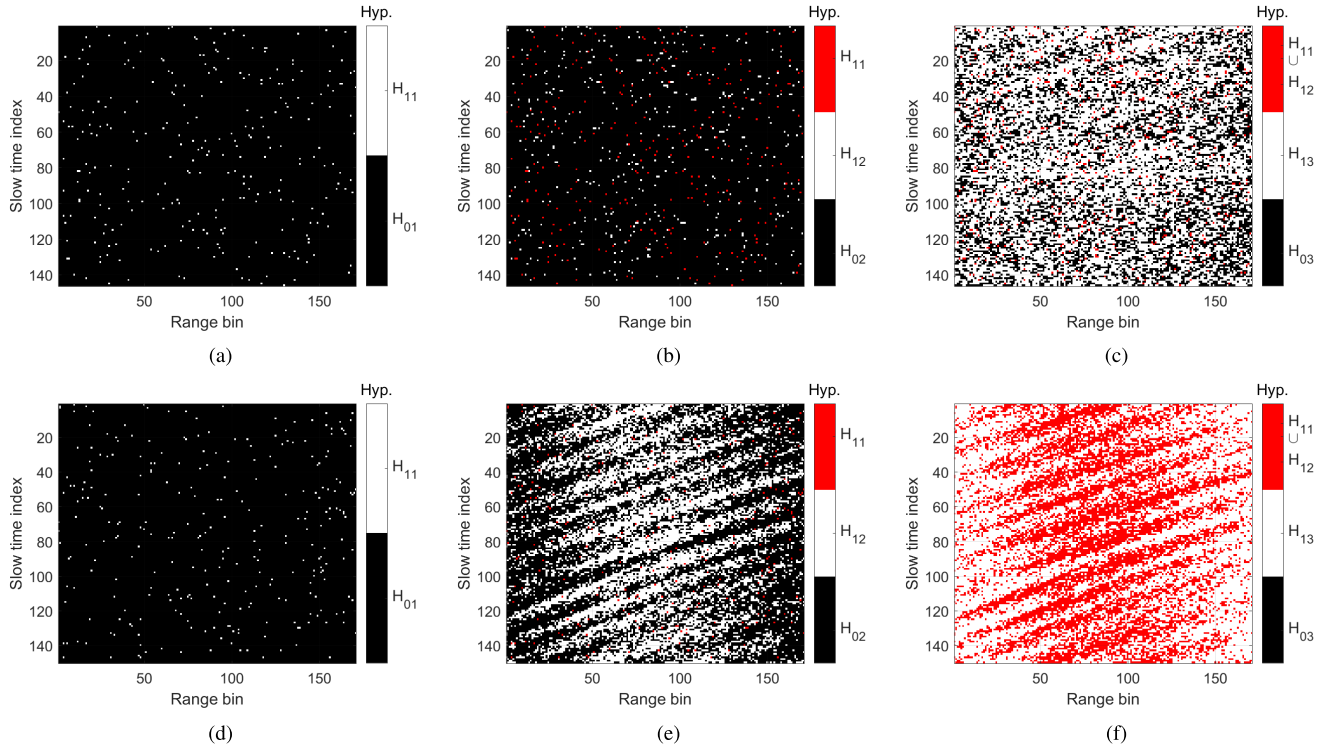

Fig. 11. Detection maps obtained using datasets 1 and 8 ($\beta = 60°$). (a)–(c) Related to dataset 1 (horizontally polarized transmission) and tests T_1, T_2, and T_3, respectively. (d)–(f) Related to dataset 8 (vertically polarized transmission) and tests T_1, T_2, and T_3, respectively.

test T_1 is applied to the whole data, whereas tests T_2 and T_3 are only applied to the observations complying with H_{01} and with both H_{01} and H_{02}, respectively. The data excluded from the testing procedures T_2 and T_3 are marked within the corresponding detection maps with H_{11} and $H_{11} \cup H_{12}$, respectively. With this premise and looking over the figures it is possible to infer that:

1) regardless of the transmit polarization and bistatic angle, most of the cross-polarized bistatic measurements can be assumed statistically independent (hypothesis H_{01});
2) the highest number of observations satisfying the hypothesis of statistically independent cross-polarized bistatic measurements sharing the same covariance matrix (hypothesis H_{03}) is obtained for $\beta = 60°$ and horizontally polarized transmission (i.e., dataset 1); and
3) regardless of the bistatic angle, using horizontally polarized transmission, the number of instances classified under the hypothesis of statistically independent cross-polarized bistatic data with proportional covariance matrices (i.e., hypothesis H_{02}) is higher than that using the vertically polarized counterpart.

The last finding is in line with the results shown in (b) and (d) of Figs. 4, 6, and 8 (for datasets 8, 11, and 12, respectively) and those reported in Table IV. More specifically, a necessary condition for the covariance matrices to be proportional/equal is that they share the same structure. However, the analyses performed in Section IV highlight that the percentages of data classified under the centrohermitian (centrosymmetric) hypothesis on the two bistatic nodes are closer for the case of horizontal transmission than for the vertical transmitted polarization.

The aforementioned trends are confirmed by the values in Table VI, which represent the average percentage of data classified under the null hypothesis for tests T_1, T_2, and T_3. These values also reveal the following trends:

1) regardless of the bistatic angle, using the vertically polarized transmission (datasets 8, 11, and 12) there are no tested data compliant with the hypothesis of statistically independent bistatic measurements sharing the same covariance matrix (H_{03}) and
2) using the horizontally polarized transmission (datasets 1, 4, and 5), the percentage of data classified under the hypotheses H_{02} and H_{03} decreases as the bistatic angle increases.

Summarizing, for all the sensing system setups, the conducted investigation highlights that within the coherence time,

$$T_1 : \begin{cases} H_{01} : \mathbf{\Sigma} \in \Theta_1 \rightarrow T_2 : \begin{cases} H_{02} : \mathbf{\Sigma} \in \Theta_2 \rightarrow T_3 : \begin{cases} H_{03} : \mathbf{\Sigma} \in \Theta_3 \\ H_{13} : \mathbf{\Sigma} \in \Theta_2 \end{cases} \\ H_{12} : \mathbf{\Sigma} \in \Theta_1 \end{cases} \\ H_{11} : \mathbf{\Sigma} \in \Theta_0 \end{cases} \tag{19}$$

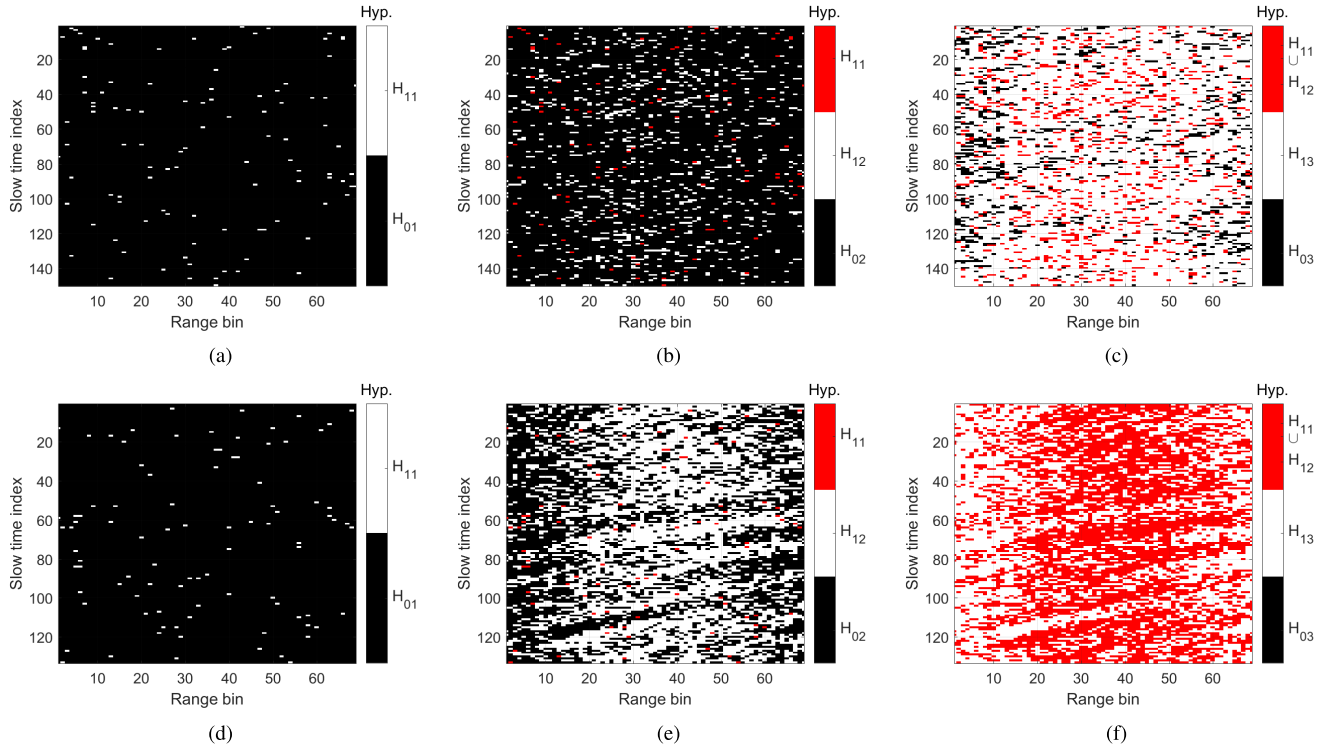

Fig. 12. Detection maps obtained using datasets 4 and 11 ($\beta = 90°$). (a)–(c) Related to dataset 4 (horizontally polarized transmission) and tests T_1, T_2, and T_3, respectively. (d), (e), and (f) Related to dataset 11 (vertically polarized transmission) and tests T_1, T_2, and T_3, respectively.

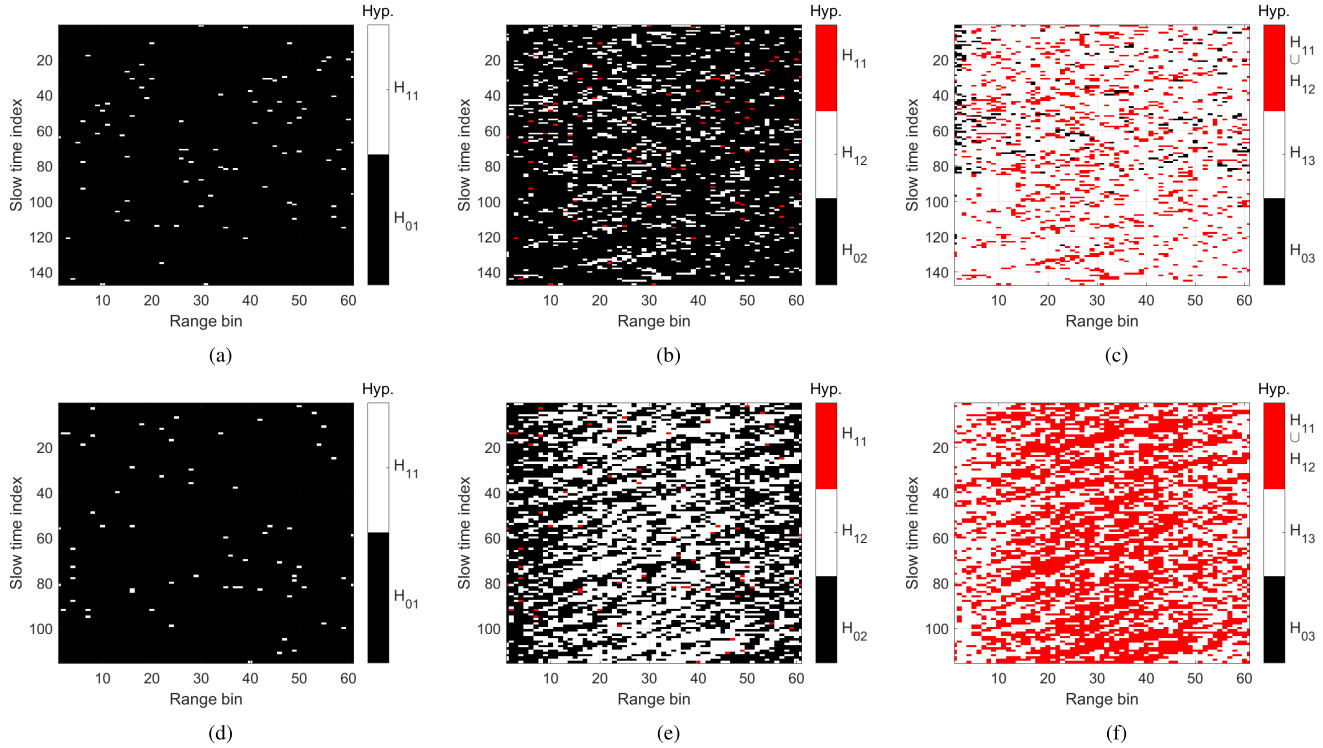

Fig. 13. Detection maps obtained using datasets 5 and 12 ($\beta = 95°$). (a)–(c) Related to dataset 5 (horizontally polarized transmission) and tests T_1, T_2, and T_3, respectively. (d)–(f) Related to dataset 12 (vertically polarized transmission) and tests T_1, T_2, and T_3, respectively.

the cross-polarized bistatic measurements can be modeled as jointly Gaussian and statistically independent. Moreover, depending on the transmit polarization and bistatic geometry they can also share the same spectral properties. This information can be capitalized on to develop an analytical model for the received signal so as to design a coherent detector that jointly uses all the signals collected from the environment.

TABLE VI
PERCENTAGE OF DATA CLASSIFIED UNDER THE NULL HYPOTHESIS FOR T_1, T_2, AND T_3

β	Dataset	H_{01}	H_{02}	H_{03}
60°	1	99	98	35
	8	99	60	0
90°	4	99	91	12
	11	99	48	0
95°	5	99	87	3
	12	99	50	0

VI. CONCLUSION

This article has addressed the stationarity and statistical independence of multistatic/polarimetric sea-clutter data considering different polarimetric/geometric scenarios. Precisely, starting from the analysis conducted in [25], the study has been first focused on establishing whether the data can be modeled as drawn from a stationary process within the coherence time. To this end, relying on suitable GIP-based statistics some necessary conditions for the slow-time data to be homogeneous have been tested by the means of the KS test and CV distance of the constructed statistics. Then, the possible presence of symmetries in the clutter covariance matrix for both the monostatic and bistatic measurements has been investigated through ad hoc statistical learning tools and the centroid of the clutter spectrum. Finally, the statistical independence of the sea-clutter bistatic returns on the different polarimetric channels along with the possible proportionality/equality of the covariance matrices have been investigated via a custom-made sequential hypothesis testing procedure.

The results from radar returns measured with the NetRAD system have shown that, independently of the sensing system configuration:

1) both monostatic and bistatic measurements can be considered stationary and locally Gaussian within the coherence time, as predicted by the SIRP model;
2) the bistatic returns on the two different polarimetric channels can be assumed jointly Gaussian and statistically independent within the coherence time;
3) the speckle generally has a covariance matrix exhibiting a centrohermitian/centrosymmetric structure; and
4) the spectral characteristics of the bistatic measurements are very similar.

In addition, depending on the transmit/receive polarization and bistatic geometry, this study has highlighted that:

1) the structure of the clutter covariance matrix can change along the slow-time dimension and among the different sensors; and
2) the speckle component for the bistatic measurements can exhibit proportional/equal covariance matrices on the two polarimetric channels.

The findings of this research activity pave the way for the development of an analytical model for designing a coherent detector that jointly exploits measurements collected simultaneously by monostatic and bistatic sensors with polarization diversity. Such model can also embed specific structures for the received signals so as to exploit, for instance, the centrohermitianity/centrosymmetry and/or the proportionality/equality of the covariance matrices associated with the speckle of the bistatic measurements. These studies are undoubtedly of interest and represent the object of current investigation.

As a final remark, it is worth emphasizing that, while some of the observed trends may be linked to the analyzed sea-clutter data, the proposed tests and methodologies are general and applicable regardless of both the system configuration (monostatic/bistatic/MIMO) and environmental conditions. They can be applied to analyze diverse experimental data (gathered from an arbitrary sensing network) and the information inferred on the clutter can be still capitalized to design coherent detectors that jointly use all the signals collected from the environment.

ACKNOWLEDGMENT

The authors are grateful to the University College London (UCL), London, U.K., and University of Cape Town (UCT), Cape Town, South Africa, teams for collecting the data and making them available for this analysis.

REFERENCES

[1] M. A. Richards, J. A. Scheer, and W. A. Holm, *Principles of Modern Radar: Basic Principles* (Radar, Sonar & Navigation). Edison, NJ, USA: Institution of Engineering and Technology, 2010.

[2] A. Aubry, A. De Maio, and A. Farina, *Polarimetric Radar Signal Processing* (Radar, Sonar and Navigation). Stevenage, U.K.: Institution of Engineering and Technology, Feb. 2023.

[3] L. Rosenberg and S. Watts, *Radar Sea Clutter: Modelling and Target Detection* (IET Radar, Sonar & Navigation). Edison, NJ, USA: Institution of Engineering and Technology, 2021.

[4] H. W. Melief, H. Greidanus, P. van Genderen, and P. Hoogeboom, "Analysis of sea spikes in radar sea clutter data," *IEEE Trans. Geosci. Remote Sens.*, vol. 44, no. 4, pp. 985–993, Apr. 2006.

[5] S. Bocquet, "Analysis and simulation of low grazing angle X-band coherent radar sea clutter using memoryless nonlinear transformations," *IEEE Trans. Geosci. Remote Sens.*, vol. 60, pp. 1–13, 2022, Art. no. 5111113.

[6] L. Rosenberg, "Parametric modeling of sea clutter Doppler spectra," *IEEE Trans. Geosci. Remote Sens.*, vol. 60, pp. 1–9, 2022, Art. no. 5105409.

[7] J. Carretero-Moya, J. Gismero-Menoyo, A. Blanco-Del-Campo, and A. Asensio-Lopez, "Statistical analysis of a high-resolution sea-clutter database," *IEEE Trans. Geosci. Remote Sens.*, vol. 48, no. 4, pp. 2024–2037, Apr. 2010.

[8] J. Carretero-Moya, J. Gismero-Menoyo, A. Asensio-Lopez, and A. Blanco-Del-Campo, "Small-target detection in high-resolution heterogeneous sea-clutter: An empirical analysis," *IEEE Trans. Aerosp. Electron. Syst.*, vol. 47, no. 3, pp. 1880–1898, Jul. 2011.

[9] G. Cui, N. Li, L. Pallotta, G. Foglia, and L. Kong, "Geometric barycenters for covariance estimation in compound-Gaussian clutter," *IET Radar, Sonar Navigat.*, vol. 11, no. 3, pp. 404–409, Mar. 2017.

[10] L. Rosenberg and Y. Abramovich, "Multi-static target detection in K-distributed sea clutter and Gaussian noise," in *Proc. IEEE Radar Conf. (RadarConf)*, May 2017, pp. 0346–0351.

[11] R. Palamà, M. Greco, and F. Gini, "Multistatic CFAR detection in non-Gaussian clutter," in *Proc. IEEE Radar Conf. (RadarConf)*, May 2016, pp. 1–6.

[12] R. Palamá, L. Rosenberg, and H. Griffiths, "Performance evaluation of two multistatic radar detectors on real and simulated sea-clutter data," in *Proc. Int. Conf. Radar (RADAR)*, Aug. 2018, pp. 1–6.

[13] H. D. Griffiths, "Keynote address: 'Clutter diversity: A new degree of freedom in multistatic radar,"' in *Proc. IEEE Radar Conf.*, May 2014, p. 11.

[14] R. Klemm, U. Nickel, C. Gierull, P. Lombardo, H. Griffiths, and W. Koch, *Novel Radar Techniques and Applications Volume 2: Waveform Diversity and Cognitive Radar, and Target Tracking and Data Fusion* (Radar, Sonar & Navigation). Edison, NJ, USA: Institution of Engineering and Technology, 2017.

[15] W. Al-Ashwal, "Measurement and modelling of bistatic sea clutter," Ph.D. dissertation, Univ. College London, London, U.K., 2011. [Online]. Available: https://discovery.ucl.ac.uk/id/eprint/1334081/

[16] W. A. Al-Ashwal, K. Woodbridge, and H. D. Griffiths, "Analysis of bistatic sea clutter—Part I: Average reflectivity," *IEEE Trans. Aerosp. Electron. Syst.*, vol. 50, no. 2, pp. 1283–1292, Apr. 2014.

[17] W. A. Al-Ashwal, K. Woodbridge, and H. D. Griffiths, "Analysis of bistatic sea clutter—Part II: Amplitude statistics," *IEEE Trans. Aerosp. Electron. Syst.*, vol. 50, no. 2, pp. 1293–1303, Apr. 2014.

[18] R. Palamà, M. S. Greco, P. Stinco, and F. Gini, "Statistical analysis of bistatic and monostatic sea clutter," *IEEE Trans. Aerosp. Electron. Syst.*, vol. 51, no. 4, pp. 3036–3054, Oct. 2015.

[19] M. Ritchie, A. Stove, K. Woodbridge, and H. Griffiths, "NetRAD: Monostatic and bistatic sea clutter texture and Doppler spectra characterization at S-band," *IEEE Trans. Geosci. Remote Sens.*, vol. 54, no. 9, pp. 5533–5543, Sep. 2016.

[20] F. Fioranelli, M. Ritchie, H. Griffiths, S. Sandenbergh, and M. Inggs, "Analysis of polarimetric bistatic sea clutter using the NetRAD radar system," *IET Radar, Sonar Navigat.*, vol. 10, no. 8, pp. 1356–1366, Oct. 2016.

[21] R. Palamà et al., "Correlation analysis of simultaneously collected bistatic and monostatic sea clutter," in *Proc. IEEE Radar Conf. (RadarConf)*, May 2017, pp. 1466–1471.

[22] L. Rosenberg, S. Watts, and M. S. Greco, "Modeling the statistics of microwave radar sea clutter," *IEEE Aerosp. Electron. Syst. Mag.*, vol. 34, no. 10, pp. 44–75, Oct. 2019.

[23] S. Bocquet, "Suzuki distributed monostatic and bistatic S-band radar sea clutter," *IEEE Trans. Aerosp. Electron. Syst.*, vol. 59, no. 1, pp. 650–659, Feb. 2023.

[24] V. Carotenuto, A. Aubry, A. De Maio, and F. Fioranelli, "Multivariate polarimetric bistatic clutter statistical analysis," in *Proc. IEEE Radar Conf. (RadarConf)*, Mar. 2022, pp. 1–6.

[25] A. Aubry, V. Carotenuto, A. De Maio, and F. Fioranelli, "Compatibility assessment of multistatic/polarimetric clutter data with the SIRP model," *IEEE Trans. Aerosp. Electron. Syst.*, vol. 59, no. 1, pp. 359–374, Feb. 2023.

[26] K. Yao, "A representation theorem and its applications to spherically-invariant random processes," *IEEE Trans. Inf. Theory*, vol. IT-19, no. 5, pp. 600–608, Sep. 1973.

[27] E. Conte and M. Longo, "Characterisation of radar clutter as a spherically invariant random process," *IEE Proc. F, Commun., Radar Signal Process.*, vol. 134, no. 2, pp. 191–197, Apr. 1987.

[28] K. D. Ward, "Compound representation of high resolution sea clutter," *Electron. Lett.*, vol. 17, no. 16, pp. 561–563, Aug. 1981.

[29] E. Conte, M. Longo, and M. Lops, "Modelling and simulation of non-Rayleigh radar clutter," *IEE Proc. F-Radar Signal Process.*, vol. 138, no. 2, pp. 121–130, Apr. 1991.

[30] E. Conte, A. de Maio, and C. Galdi, "Statistical analysis of real clutter at different range resolutions," *IEEE Trans. Aerosp. Electron. Syst.*, vol. 40, no. 3, pp. 903–918, Jul. 2004.

[31] K. J. Sangston and K. R. Gerlach, "Coherent detection of radar targets in a non-Gaussian background," *IEEE Trans. Aerosp. Electron. Syst.*, vol. 30, no. 2, pp. 330–340, Apr. 1994.

[32] H. Song, Y. Sun, R. Wang, W. Fei, Y. Wang, and J. Wang, "Phase estimation of distributed scatterer for high resolution data stacks in nonurban areas," in *Proc. IEEE Int. Geosci. Remote Sens. Symp. (IGARSS)*, Jul. 2016, pp. 5967–5970.

[33] H. Song et al., "Statistically homogeneous pixel selection for small SAR data sets based on the similarity test of the covariance matrix," *Remote Sens. Lett.*, vol. 8, no. 10, pp. 927–936, Oct. 2017.

[34] V. Carotenuto, A. Aubry, A. De Maio, and F. Fioranelli, "Exploring homogeneity and covariance matrix structure of multistatic/polarimetric sea-clutter data," in *Proc. IEEE 10th Int. Workshop Metrology Aerosp. (MetroAeroSpace)*, Jun. 2023, pp. 401–406.

[35] W. A. Al-Ashwal et al., "Statistical analysis of simultaneous monostatic and bistatic sea clutter at low grazing angles," *Electron. Lett.*, vol. 47, no. 10, p. 621, 2011.

[36] W. A. Al-Ashwal et al., "Measurements of bistatic radar sea clutter," in *Proc. IEEE RadarCon (RADAR)*, May 2011, pp. 217–221.

[37] H. Griffiths, "Developments in bistatic and networked radar," in *Proc. IEEE CIE Int. Conf. Radar*, vol. 1, Oct. 2011, pp. 10–13.

[38] M. A. Ritchie, W. A. Al-Ashwal, A. G. Stove, K. Woodbridge, and H. D. Griffiths, "Statistical analysis of monostatic and bistatic sea clutter Doppler spectrum," in *Proc. IEEE CIE Int. Conf. Radar*, vol. 1, Oct. 2011, pp. 816–820.

[39] R. Palamà, M. Greco, P. Stinco, and F. Gini, "Statistical analysis of netrad high resolution sea clutter," in *Proc. 21st Eur. Signal Process. Conf. (EUSIPCO)*, Sep. 2013, pp. 1–5.

[40] M. A. Ritchie, W. A. Al-Ashwal, A. G. Stove, K. Woodbridge, and H. D. Griffiths, "Coherent analysis of horizontally-polarized monostatic and bistatic sea clutter," in *Proc. IET Int. Conf. Radar Syst. (Radar)*, Oct. 2012, pp. 1–5.

[41] R. Palamà, M. Greco, P. Stinco, and F. Gini, "Analysis of sea spikes in NetRad clutter," in *Proc. 11th Eur. Radar Conf.*, Oct. 2014, pp. 109–112.

[42] S. Angelliaume, L. Rosenberg, and M. Ritchie, "Analysis of bistatic radar sea clutter amplitude distributions at low grazing angles," in *Proc. Int. Radar Conf. (RADAR)*, Sep. 2019, pp. 1–5.

[43] P. Wang, H. Li, and B. Himed, "Moving target detection using distributed MIMO radar in clutter with nonhomogeneous power," *IEEE Trans. Signal Process.*, vol. 59, no. 10, pp. 4809–4820, Oct. 2011.

[44] C. Y. Chong, F. Pascal, J.-P. Ovarlez, and M. Lesturgie, "MIMO radar detection in non-Gaussian and heterogeneous clutter," *IEEE J. Sel. Top. Signal Process.*, vol. 4, no. 1, pp. 115–126, Feb. 2010.

[45] D.-X. Yue, F. Xu, A. C. Frery, and Y.-Q. Jin, "Synthetic aperture radar image statistical modeling—Part one-single-pixel statistical models," *IEEE Geosci. Remote Sens. Mag.*, vol. 9, no. 1, pp. 82–114, Mar. 2021.

[46] D.-X. Yue, F. Xu, A. C. Frery, and Y. Jin, "Synthetic aperture radar image statistical modeling—Part two-spatial correlation models and simulation," *IEEE Geosci. Remote Sens. Mag.*, vol. 9, no. 1, pp. 115–138, Mar. 2021.

[47] L. Pralon, G. Vasile, M. D. Mura, A. Anghel, and J. Chanussot, "Spherical symmetry of complex stochastic models in multivariate high-resolution PolSAR images," *IEEE Trans. Geosci. Remote Sens.*, vol. 54, no. 7, pp. 4250–4261, Jul. 2016.

[48] P. Formont, F. Pascal, G. Vasile, J.-P. Ovarlez, and L. Ferro-Famil, "Statistical classification for heterogeneous polarimetric SAR images," *IEEE J. Sel. Topics Signal Process.*, vol. 5, no. 3, pp. 567–576, Jun. 2011.

[49] V. Carotenuto, A. De Maio, D. Orlando, and P. Stoica, "Radar detection architecture based on interference covariance structure classification," *IEEE Trans. Aerosp. Electron. Syst.*, vol. 55, no. 2, pp. 607–618, Apr. 2019.

[50] J. Xue, S. Xu, and J. Liu, "Persymmetric detection of radar targets in nonhomogeneous and non-Gaussian sea clutter," *IEEE Trans. Geosci. Remote Sens.*, vol. 60, pp. 1–9, 2022, Art. no. 5103709.

[51] Z. Wang, Z. He, Q. He, B. Xiong, and Z. Cheng, "Persymmetric adaptive target detection with dual-polarization in compound Gaussian sea clutter with inverse gamma texture," *IEEE Trans. Geosci. Remote Sens.*, vol. 60, pp. 1–17, 2022, Art. no. 5118117.

[52] J. T. Nohara, "Detection of growlers in sea clutter using an X-band pulse-Doppler radar," Ph.D. dissertation, McMaster Univ., Hamilton, ON, Canada, 1991. [Online]. Available: https://macsphere.mcmaster.ca/handle/11375/8499

[53] M. Rangaswamy, J. H. Michels, and B. Himed, "Statistical analysis of the non-homogeneity detector for STAP applications," *Digit. Signal Process.*, vol. 14, no. 3, pp. 253–267, May 2004.

[54] M. C. Wicks, Y. Zhang, and R. Schneible, "A generalized inner product based algorithm for improved detection and discrimination of over resolved targets in MIMO radar," in *Proc. 8th Eur. Conf. Synth. Aperture Radar*, Jun. 2010, pp. 1–4.

[55] W. L. Melvin, M. C. Wicks, and R. D. Brown, "Assessment of multichannel airborne radar measurements for analysis and design of space-time processing architectures and algorithms," in *Proc. IEEE Nat. Radar Conf.*, May 1996, pp. 130–135.

[56] R. D'Agostino and M. Stephens, *Goodness-of-Fit Techniques*. New York, NY, USA: Marcel Dekker, 1986.

[57] V. Carotenuto, A. De Maio, D. Orlando, and P. Stoica, "Model order selection rules for covariance structure classification in radar," *IEEE Trans. Signal Process.*, vol. 65, no. 20, pp. 5305–5317, Oct. 2017.

[58] D. Ramírez, J. Via, I. Santamaría, and L. L. Scharf, "Detection of spatially correlated Gaussian time series," *IEEE Trans. Signal Process.*, vol. 58, no. 10, pp. 5006–5015, Oct. 2010.

[59] V. Carotenuto, A. De Maio, C. Clemente, and J. J. Soraghan, "Invariant rules for multipolarization SAR change detection," *IEEE Trans. Geosci. Remote Sens.*, vol. 53, no. 6, pp. 3294–3311, Jun. 2015.

[60] V. Carotenuto, A. De Maio, C. Clemente, J. J. Soraghan, and G. Alfano, "Forcing scale invariance in multipolarization SAR change detection," *IEEE Trans. Geosci. Remote Sens.*, vol. 54, no. 1, pp. 36–50, Jan. 2016.

[61] D. P. Bertsekas, "Nonlinear programming," *J. Oper. Res. Soc.*, vol. 48, no. 3, p. 334, 1997.

[62] A. Wiesel, "Geodesic convexity and covariance estimation," *IEEE Trans. Signal Process.*, vol. 60, no. 12, pp. 6182–6189, Dec. 2012.

Augusto Aubry (Senior Member, IEEE) received the Dr.Eng. degree (Hons.) in telecommunication engineering and the Ph.D. degree in electronic and telecommunication engineering from the University of Naples Federico II, Naples, Italy, in 2007 and 2011, respectively.

From February 2012 to April 2012, he was a Visiting Researcher with the Hong Kong Baptist University, Hong Kong. He is currently an Associate Professor with the University of Naples Federico II. His research interests include statistical signal processing and optimization theory, with emphasis on MIMO communications and radar signal processing.

Dr. Aubry was a co-recipient of the 2013 Best Paper Award (titled to B. Carlton) of IEEE TRANSACTIONS ON AEROSPACE AND ELECTRONIC SYSTEMS with the contribution "Knowledge-Aided (Potentially Cognitive) Transmit Signal and Receive Filter Design in Signal-Dependent Clutter." He was a recipient of the 2022 IEEE Fred Nathanson Memorial Award as the Young (less than 40 years of age) AESS Radar Engineer 2022, with the following citation "for outstanding contributions to the application of modern optimization theory to radar waveform design and adaptive signal processing."

Vincenzo Carotenuto (Senior Member, IEEE) received the Dr.Eng. degree in telecommunication engineering and the Ph.D. degree in electronic and telecommunication engineering from the University of Naples Federico II, Naples, Italy, in 2010 and 2015, respectively.

From September 2022 to December 2022, he was a Visiting Researcher with the Delft University of Technology, Delft, The Netherlands. He is currently under a research agreement with the University of Naples Federico II. His research interests include the field of statistical signal processing, with an emphasis on radar signal processing.

Dr. Carotenuto was a co-recipient of the Best Radar Paper Award of the 2018 IEEE International Workshop on Metrology for Aerospace with the contribution "Assessing Spectral Compatibility Between Radar and Communication Systems on Measured Data."

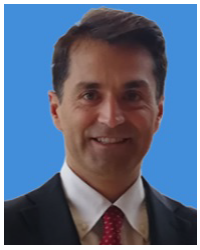

Antonio De Maio (Fellow, IEEE) received the Dr.Eng. (Hons.) and Ph.D. degrees in information engineering from the University of Naples Federico II, Naples, Italy, in 1998 and 2002, respectively.

From October 2004 to December 2004, he was a Visiting Researcher with the U.S. Air Force Research Laboratory, Rome, NY, USA. From November 2007 to December 2007, he was a Visiting Researcher with The Chinese University of Hong Kong, Hong Kong. He is currently a Professor with the University of Naples Federico II. His research interests include the field of statistical signal processing, with emphasis on radar detection, optimization theory applied to radar signal processing, and multiple-access communications.

Dr. De Maio was a recipient of the 2010 IEEE Fred Nathanson Memorial Award as the Young (less than 40 years of age) AESS Radar Engineer 2010 whose performance is particularly noteworthy as evidenced by contributions to the radar art over a period of several years, with the following citation for "robust CFAR detection, knowledge-based radar signal processing, and waveform design and diversity." He was a co-recipient of the 2013 Best Paper Award (titled to B. Carlton) of IEEE TRANSACTIONS ON AEROSPACE AND ELECTRONIC SYSTEMS with the contribution "Knowledge-Aided (Potentially Cognitive) Transmit Signal and Receive Filter Design in Signal-Dependent Clutter."

Francesco Fioranelli (Senior Member, IEEE) received the Ph.D. degree from Durham University, Durham, U.K., in 2014.

He was an Assistant Professor with the University of Glasgow, Glasgow, U.K., from 2016 to 2019, and a Research Associate at University College London, London, U.K., from 2014 to 2016. He is currently an Associate Professor at TU Delft, Delft, The Netherlands. His research interests include the development of radar systems and automatic classification for human signatures analysis in healthcare and security, drone and UAV detection and classification, automotive radar, wind farms, and sea clutter.

Open Access funding provided by 'Università degli Studi di Napoli "Federico II"' within the CRUI CARE Agreement